RSC Sustainability

ROYAL SOCIETY OF CHEMISTRY

PAPER

View Article Online
View Journal

Cite this: DOI: 10.1039/d5su00859j

Green synthesis of a water-stable thiol-decorated Zr-MOF for selective heavy metal removal

Hager G. Abdel-Mohey,[ab] Worood A. El-Mehalmey,[a] Mohamed A. Seleem,[cd] Abdelrahman S. Mayhoub,[cd] Hany I. Mohmed,[b] Wagdy I. El-Dougdoug,[b] Ahmad Baraka[e] and Mohamed H. Alkordi *[a]

A green, water-based synthesis of thiol-decorated, Zr-carboxylate metal–organic framework is reported. A mixture of capping and bridging, thiol containing, organic linker approach utilizing mercaptoacetic acid (MA) and mercaptosuccinic acid (MSA) resulted in an open Zr-based MOF with thiol-decorated cages (Zr-MSA-MA MOF). Tailoring the nanospace within the micropores of water-synthesized and water-stable MSA-MOF led to several desirable attributes including: (i) chemical stability in aqueous media due to strong $-CO_2-Zr(IV)$ linkage, (ii) tight pore system leading to optimized electronic interactions with guest ions, and (iii) thiol-functionalized cages that affect selective capture of soft metal ions. The Zr-MSA-MA MOF demonstrated exceptionally high capacity for Cd (370.4 (±35.5) mg g^{-1}, 3.29 mmol g^{-1}) and Pb (500 (±16.8) mg g^{-1}, 2.41 mmol g^{-1}). It also exhibited remarkable stability indicated by its ability to regenerate and reuse the MSA-MOF for 10 consecutive cycles with nearly 95% retention of initial activity towards heavy metal removal. Moreover, the thiol-decorated MOF demonstrated high selectivity for Pb and Cd in the presence of competing Cu, Zn, Ni, Mn, Fe, and Co ions. These findings highlight the potential of Zr-MSA-MA MOF as a highly efficient, selective, and regenerable sorbent for heavy metal remediation.

Received 11th November 2025
Accepted 19th February 2026

DOI: 10.1039/d5su00859j

rsc.li/rscsus

Sustainability spotlight

This work demonstrates the utilization of green synthesis by reporting a sustainable, water-based synthesis of a thiol-decorated zirconium MOF. This method eliminates toxic solvents commonly utilized in the synthesis of MOFs, aligning with the principles of green chemistry. The reported material directly addresses SDG 6 (Clean Water and Sanitation) by serving as a highly efficient, selective, and regenerable sorbent for toxic heavy metals like lead and cadmium. Its exceptional reusability over multiple cycles, besides high selectivity for heavy metals, promotes SDG 12 (Responsible Consumption and Production) by minimizing waste. By providing a robust tool for industrial wastewater treatment, this research offers a tangible solution to reduce water pollution and its harmful impacts on ecosystems and human health.

Introduction

The global scarcity of freshwater necessitates sustainable practices for the utilization of the available water resources. It is becoming globally accepted that such practices should include reducing waste discharge at the source, recycling used water whenever possible, and reusing industrial wastewater to alleviate the demand on freshwater sources.[1–3] Among the different kinds of water contaminants, heavy metal ions are associated with severe environmental and health problems. Heavy metal ions such as Cd, Pb, and Cr are prevalent in waste streams from several industries including the cement industry, mining, chrome electroplating, battery manufacturing, and leather tanning.[4] Such heavy metal ions are non-biodegradable, leading to their accumulation in the food chain, with paramount toxicity to human as well as plants and aquatic life. Prolonged exposure to heavy metals is known to induce various health disorders such as kidney damage, bone fractures, and neurological impairment, among others.[5] Therefore, effective and efficient removal of these contaminants from wastewater is critical for sustainable industrial practices and environmental protection.

Conventional methods for heavy metal removal from water conventionally include (i) chemical precipitation, (ii) ion exchange, (iii) membrane filtration, and (iv) electrochemical treatment. Although chemical precipitation is commonly used due to its simplicity and cost-effectiveness, it is often associated

[a]Center for Material Science, Zewail City of Science and Technology, Giza 12578, Egypt
[b]Chemistry Department, Faculty of Science, Benha University, Benha 13518, Egypt
[c]Department of Pharmaceutical Organic Chemistry, Faculty of Pharmacy, Al-Azhar University, Cairo 11884, Egypt
[d]Center of Certified Reference Materials, Zewail City of Science and Technology, Giza 12578, Egypt
[e]Department of Chemical Engineering, Military Technical College, Cairo, Egypt. E-mail: malkordi@zewailcity.edu.eg

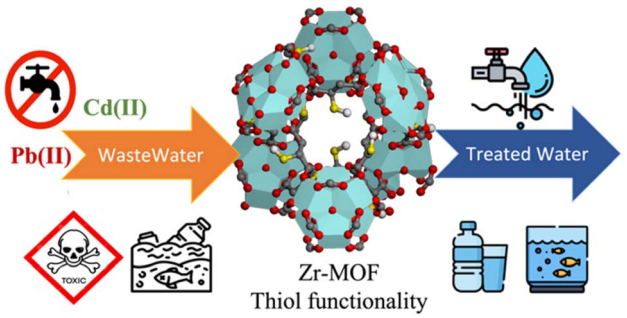

Scheme 1 Illustrative scheme for wastewater treatment by selective and regenerable Zr-MSA-MA MOF.

with the production of a large volume of sludge, which requires additional treatment and handling. Ion exchange technology offers high specificity in metal removal, but its application is limited by the need for complex regeneration procedures and high operational costs. Membrane filtration provides excellent separation efficiency but is constrained by membrane fouling and high energy requirements typically associated with high pressure operating conditions. Electrochemical treatments, known for their potential in heavy metal recovery, are hindered by high energy consumption and operational complexity, primarily due to the need for specialized electrochemical cell design and operation. In summary, the abovementioned technologies are faced with certain challenges, stimulating interest for the adsorptive removal of heavy metals into porous solids.[5–9]

Microporous solids hold great promise as sorbent materials for the adsorptive removal of water-soluble organic dyes,[10,11] as well as soluble heavy metal ions from wastewater.[12–15] Key attributes of such materials are the high surface area and the tailorable chemical composition of such solids.[16] Metal–organic frameworks (MOFs) based on Zr(IV)-carboxylate demonstrated both high chemical stability in an aqueous environment, as well as high modality associated with the large chemical space of the organic linkers.[17–19] Herein, we demonstrate that utilizing the robust –CO_2–Zr(IV) bonding in Zr-MOFs, alongside careful tailoring of the cage dimensions as well as presence of soft-base thiol functional groups decorating the micropores within the porous solid, resulted in notable activity of a porous material. The mixed linker MOF containing mercaptosuccinate-mercaptoacetate Zr(IV) MOF (Zr-MSA-MA MOF) reported herein demonstrated high capacity and selective uptake towards Pb(II) and Cd(II) ions, even in the presence of other transition metal ions like Cu(II), Zn(II), Co(II), Fe(III), and Mn(II). Key to this approach is the functionalization of the nanospace within the cages by employing the thiol groups as tethering sites for soft metals, while simultaneously adjusting the pore dimensions through utilization of mixed linkers, mercaptosuccinic and mercaptoacetic acid.

The greenness of our synthesis is highlighted by utilizing an aqueous solution, circumventing the commonly utilized toxic and/or volatile organic solvents commonly used in MOF synthesis.[20] On the CHEM21 solvent selection scale,[21] replacing high-burden organic media with water reduces the environmental and health impact scores to their lowest possible values, representing nearly 91% reduction in production-related environmental burdens.[22] Besides enhancing safety and sustainability of the production of such desirable MOF, this method also offers a scalable, cost-effective pathway that is anticipated to positively impact commercialization of such a material in the

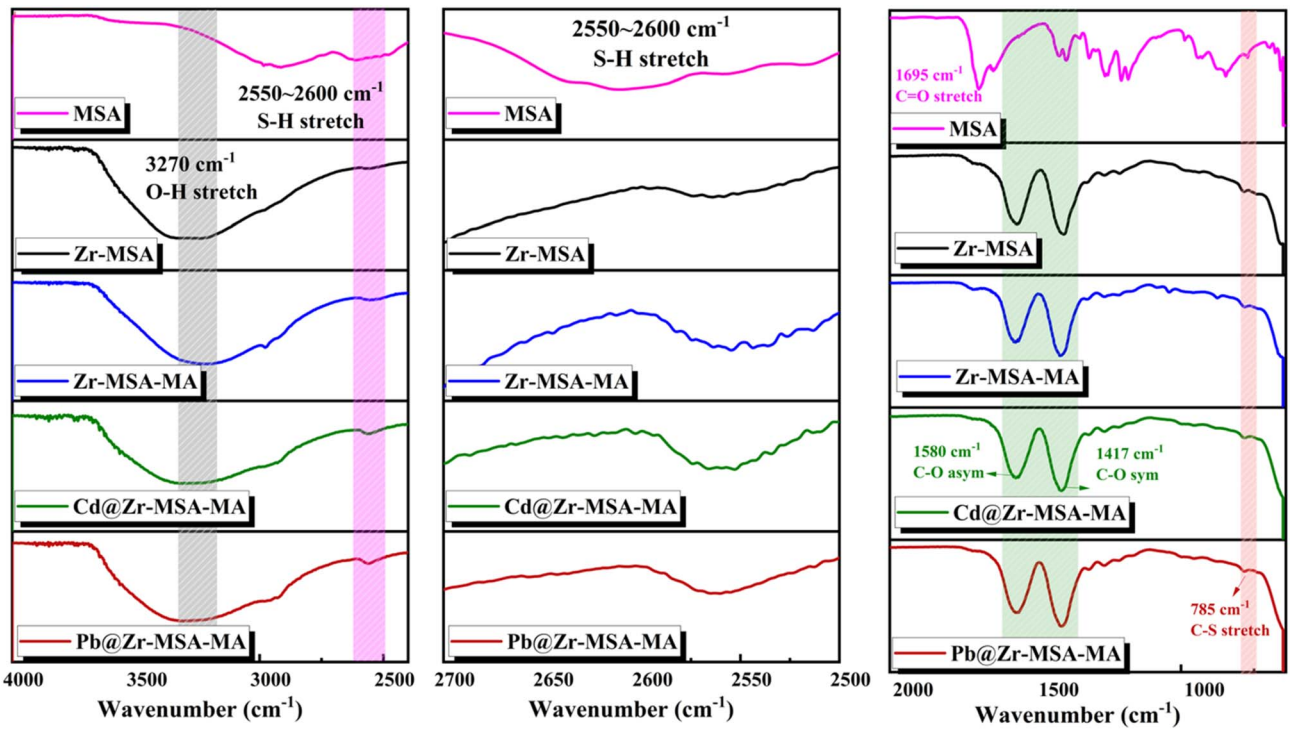

Fig. 1 FTIR spectra of mercaptosuccinic acid ligand, Zr-MSA, Zr-MSA-MA, Cd@Zr-MSA MA, and Pb@Zr-MSA-MA.

near future. Additionally, utilization of water as the solvent can greatly enhance the scalability and reproducibility of the synthesis by alleviating dependence on solvent grade, purity, or supplier.

Results and discussion

Mixed-Linker Zr-based MOF Synthesis and Characterization. This study utilized tailored synthesis of the mercaptosuccinic acid (MSA) Zr-MOF, where mercaptoacetic acid (MA) was deliberately added to the synthesis to introduce defect sites of open/loose end linkers in combination with bridged Zr(IV) clusters yielding a crystalline solid, herein termed Zr-MSA-MA MOF (**1**), Scheme 1.[23] The Fourier transform infrared (FTIR) spectra in Fig. 1 indicated enhanced S–H stretching absorption at ~2550 cm^{-1} when mercaptoacetic acid was used to construct **1**, as compared to the relative intensity of S–H stretching observed in the pristine Zr-MSA MOF. Upon incubation of **1** into the solution of various heavy metal ions, the characteristic absorption for free S–H stretching is far diminished compared to that in the MSA linker, indicating S–Cd and S–Pb coordination to the heavy metal ions Cd(II) and Pb(II), within the Zr-MSA-MA framework. The FTIR spectrum of free MSA showed a distinct S–H stretching band at ~2600 cm^{-1}, characteristic of a free, uncoordinated thiol group. Moreover, the C–S stretching band at ~785 cm^{-1} is observed in all solids, confirming the

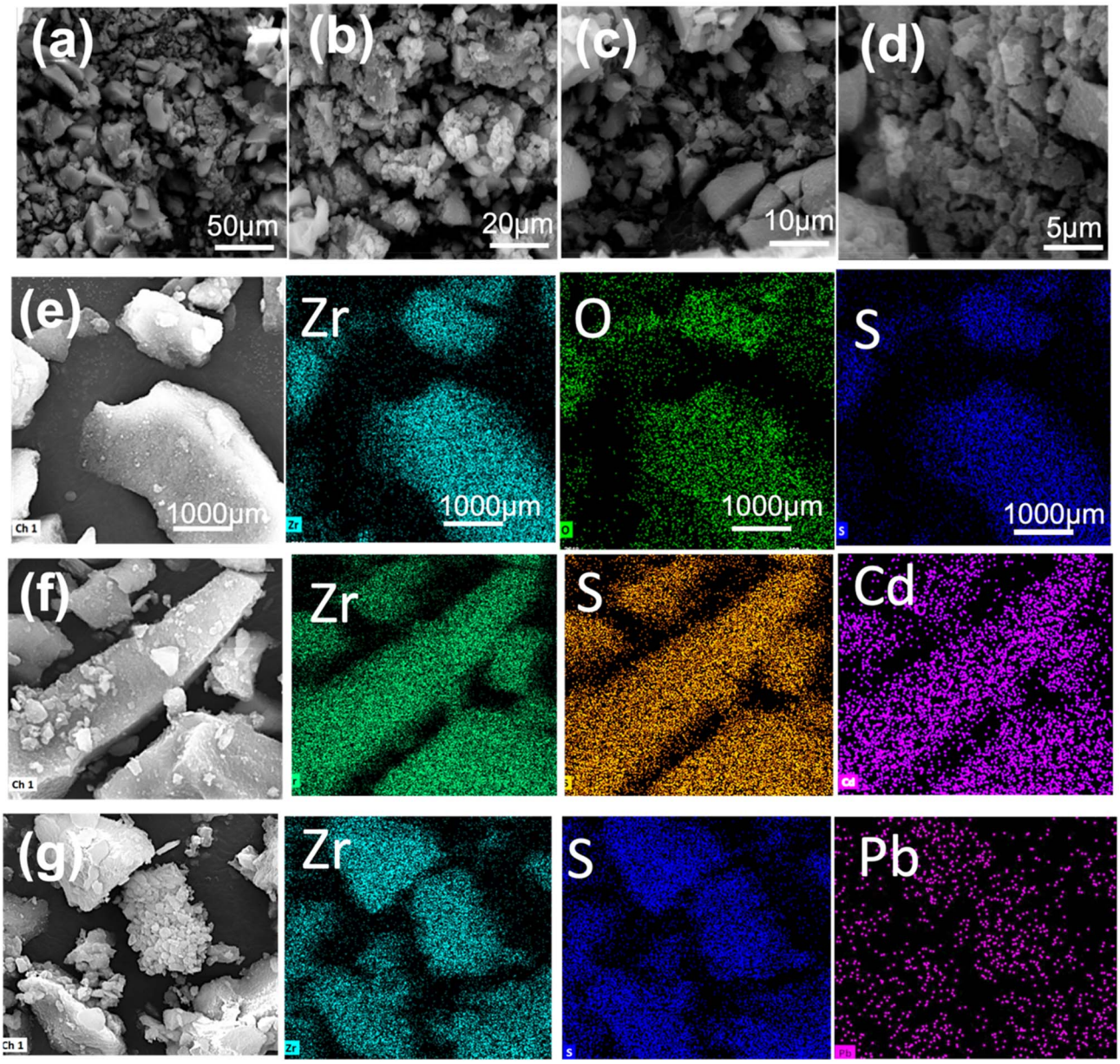

Fig. 2 (a–d) Scanning electron microscopy (SEM) images of the Zr-MSA-MA MOF, (e) SEM and EDX mapping for the pristine MOF, (f) SEM and EDX mapping after Cd(II) uptake, and (g) after Pb(II) uptake demonstrating homogeneous distribution of the Zr, S, Cd, and Pb elements within the samples.

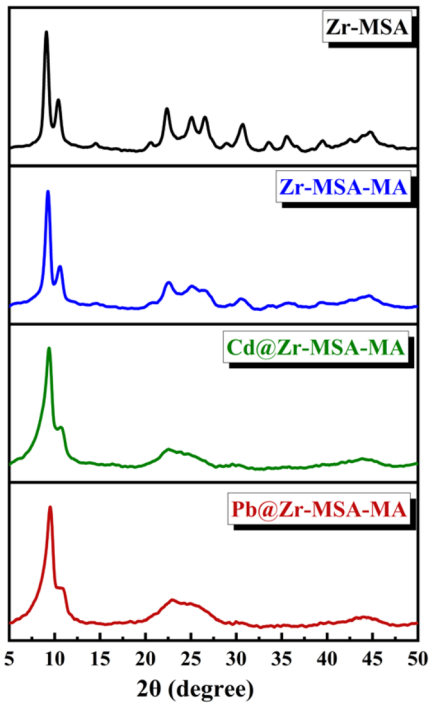

Fig. 3 XRD patterns of Zr-MSA-MOF, Zr-MSA-MA MOF, Cd@Zr-MSA-MA-MOF, and Pb@ Zr-MSA-MA-MOF.

presence of thiolated linkers within the isolated solids. The C═O stretching band, initially observed at ~1695 cm^{-1} in free MSA, experienced a notable red shift toward lower wavenumbers, as well as the prominent appearance of the asymmetric and symmetric COO^- bands at 1580 cm^{-1} and 1417 cm^{-1}, respectively, strongly confirming the formation of metal-carboxylate interactions involved in $-CO_2-Zr(IV)$ linkage.

The scanning electron microscopy images in Fig. 2 demonstrated the block-shaped crystallites of the Zr-MSA-MA MOF, **1**. Additionally, energy-dispersive X-ray mapping (EDX) in Fig. 2, for the pristine crystals of **1** and after soaking into solutions of Pb(II) and Cd(II) salts, clearly demonstrated the homogeneous distribution of sulfur, present in the thiolated linkers, as well as demonstrating homogeneous distribution of the corresponding heavy metal ions.

Crystallinity of the isolated **1** was evident utilizing X-ray diffraction patterns (XRD) for the MOF before and after treatment with the different heavy metal ions, Fig. 3. Additionally, due to the similarity between succinic acid, mercaptosuccinic acid, and aspartic acid linkers, the XRD pattern of **1** closely resembled that of the previously published homologues prepared with mercaptosuccinic acid or aspartic acid linkers.[14,24] A mild amorphization is observed when comparing the XRD patterns of **1** utilizing the terminal MA ligand added to the reaction mixture to induce defect sites, as compared to the more crystalline nature of the single ligand system, mercaptosuccinic acid, Fig. 3, and is expected due to partial loss of long-range order especially at the higher theta values corresponding to pore symmetry in the material. The strongest intensity XRD peaks observed at $2\theta = 8.6°$ and 9.9° correspond to the *hkl* planes (111) and (200), respectively. The (111) plane bisects the

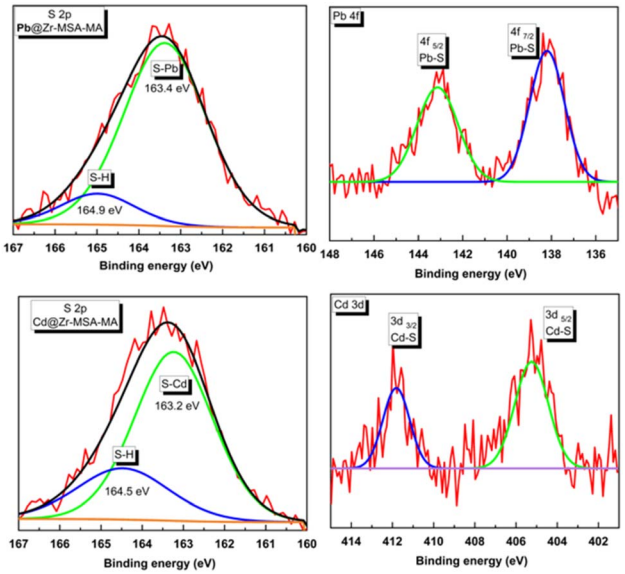

Fig. 4 XPS detailed line spectra of S 2p, Cd 3d, and Pb 4f in the Cd(II) and Pb(II) treated crystals of **1** indicating thiolate-metal coordination.

cages of the MOF passing midway between the $Zr–CO_2$ clusters, while the (200) plane represents the plane at which 4 out of the 6 Zr ions in the Zr clusters reside. After exposure to the heavy metal ions, the XRD patterns do indeed demonstrate even more visible amorphization, but overall maintained crystallinity, a strong indication of subtle but detectable changes to the pore systems due to heavy metal uptake into the pores of **1**. The incorporation of the bridging linker, mercaptosuccinic acid, in less than an equimolar ratio to the Zr(IV) ions, aided by the addition of mercaptoacetic acid, was deliberately attempted. While a purely mercaptosuccinic acid MOF provides a tight pore system, especially valuable for metal ion capture from aqueous solution, introducing linker defects through utilization of mercaptoacetic acid provided the means to open the pores more for free metal diffusion while still preserving the thiol functional groups to interact with soft metal ions like Cd, Hg, and Pb. On the other hand, attempting to synthesize the MOF solely from mercaptosuccinic acid inevitably results in encumbered cages with diminished pore window to allow for facilitated diffusion of guest ions. Therefore, our strategy was to induce the formation of partially encapsulated nanocages, fulfilling three major design principles namely: (i) chemical stability in aqueous media due to strong $CO_2–Zr(IV)$ linkage, (ii) tight pore system leading to optimized electronic interactions with guest ions, and (iii) thiol-functionalized cages to affect selective capture of soft metal ions. X-ray photoelectron spectroscopy (XPS) is a powerful tool to probe the local chemical environment of the elements, and therefore was utilized to gain more insight into the underlying mechanism for metal ion uptake by **1**. The detailed line spectra of S 2p, Cd 3d, and Pb 4f are shown in Fig. 4, demonstrating clear thiolate-metal coordination. The S 2p envelope can readily be deconvoluted into two peaks, a major peak at low binding energy (163.2–163.4 eV) corresponding to heavy metal-thiolate coordination,[25] and a minor peak at higher binding energy (164.5–164.9 eV) ascribed to the free (–SH) thiol

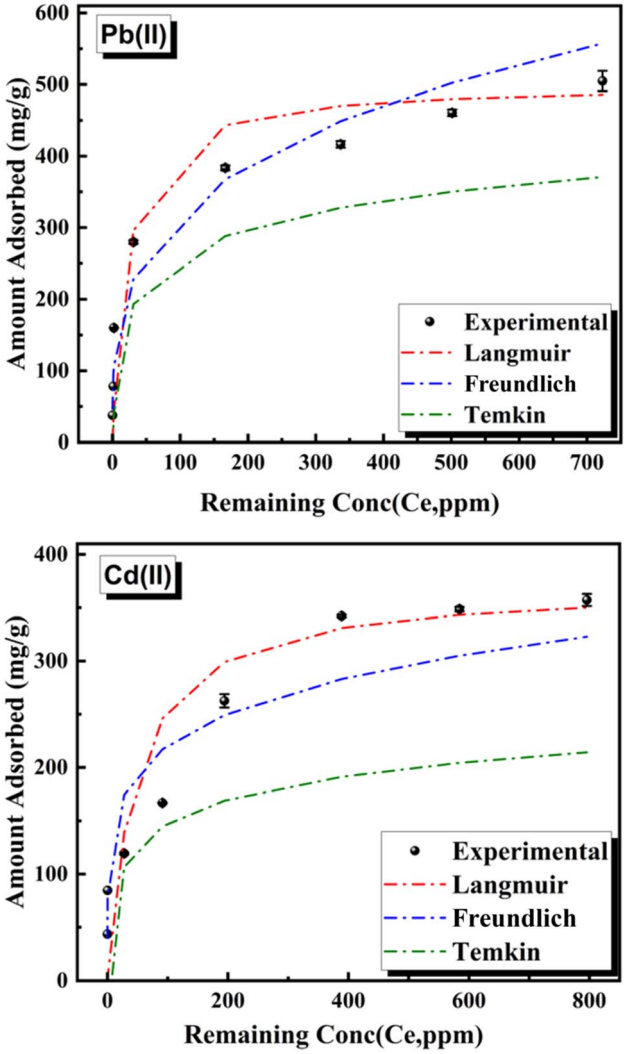

Fig. 5 Adsorption isotherms for Pb(II) and Cd(II) in **1**, experimental data points and fitting by three models (Langmuir, Freundlich, and Temkin) are shown for comparison.

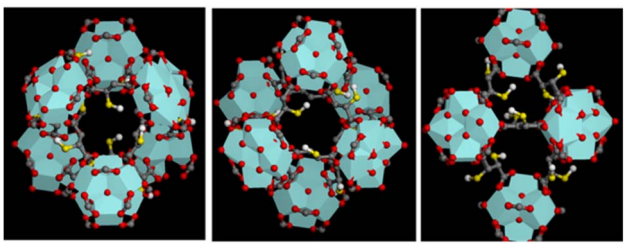

Fig. 6 Model crystal structure of the structural analogue Zr-aspartate MOF,[30] replacing $-NH_2$ in aspartate linkers by –SH groups to demonstrate the orientation within the cages.

groups[25] present within the pores of the MOF. This observation pointed to an established equilibrium between metal-coordinated thiolate (major component) and free thiol groups (minor component) within the pores of the MOF. The Cd 3d line demonstrated the characteristic spin–orbit splitting where the Cd $3d_{5/2}$ recorded at a binding energy of 405 eV was associated

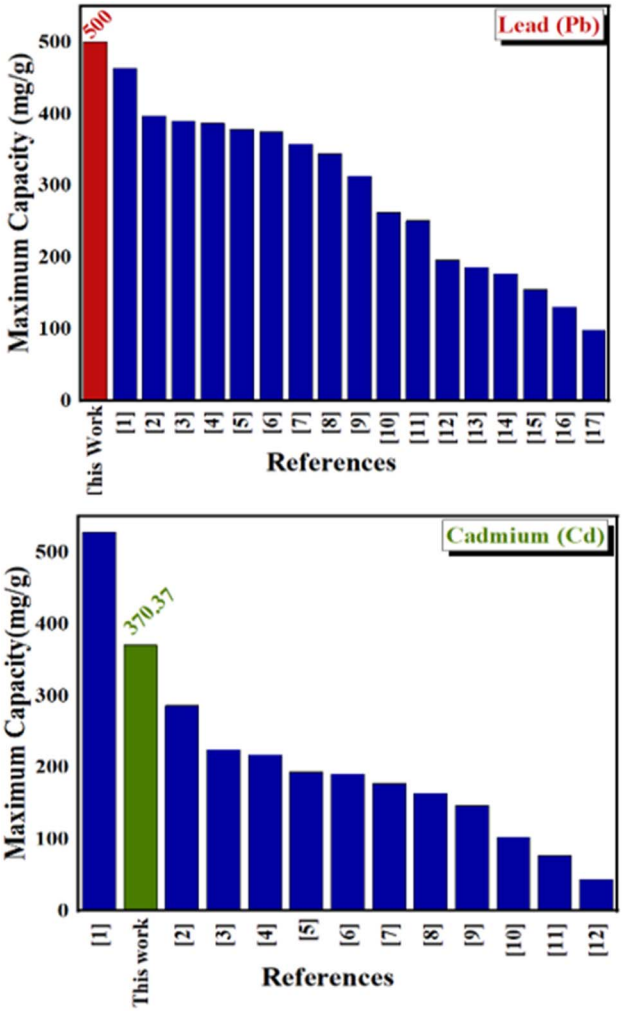

Fig. 7 Comparison of the heavy metal uptake capacity of **1** towards Pb(II) and Cd(II) to previously reported similar systems, colored bar indicated the capacity of **1**, references are listed in the SI.

with Cd–S coordination.[26] In a similar manner, the Pb $4f_{7/2}$ recorded at 138 eV is characteristic of Pb–S coordination.[27]

Zr-MSA-MA MOF uptake capacity towards Cd(II) and Pb(II)

The adsorption isotherms for Cd(II) and Pb(II) in the thiol-decorated Zr-MOF are shown in Fig. 5, along with data fitting utilizing the three common adsorption models, Langmuir, Freundlich, and Temkin models. Isotherms were collected at pH 6 determined to be the optimal solution pH; see the pH study below. Detailed parameters of the three fitted models are provided in the SI. The data fitting clearly revealed that the Langmuir model provided the best fit with the sorption isotherms for both metal ions, with high correlation coefficients ($R^2 > 0.98$). This observation indicated monolayer adsorption at homogeneously distributed binding sites, where better correlation between the experimental and calculated capacity utilizing the Langmuir model suggested that the adsorption sites within the MOF are energetically uniform, and interactions with binding sites occur without multilayer formation. The calculated maximum adsorption capacities (q_m) were 500

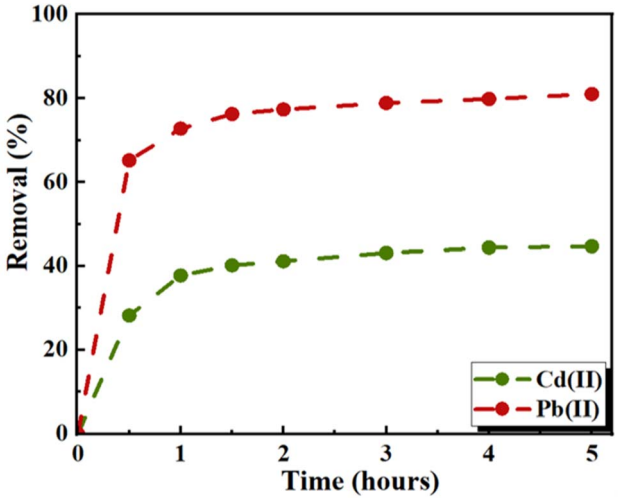

Fig. 8 Time-dependence investigation of the heavy metal removal by **1** indicating rapid removal within a 30 minutes contact time, reaching equilibrium at 90 minutes.

(±16.8) mg g^{-1} for Pb(II), and 370.4 (±35.5) mg g^{-1} for Cd(II) ions. While, at first glance, such values do not seem to outline any underlying relationship between the type of heavy metal and the MOF capacity for that metal ion, closer inspection revealed a decreasing capacity in terms of mmol g^{-1} in the order of Cd(II) (3.29 mmol g^{-1}) to Pb(II) (2.41 mmol g^{-1}). Interestingly, we note that ionic radii of the ions investigated follow the order of Cd(II) (0.95–1.1 Å) to Pb(II) (1.1 Å).[28,29] This observation can be explained considering the relationship between the average radius of the metal ion hydration shell, and overall uptake capacity within **1**. We postulate that this relationship underpins diffusivity of the hydrated metal ions within the pores of the MOF, thereby affecting the observed uptake capacity of **1** towards Cd(II) and Pb(II) ions. The tight pore systems present in a model generated by utilizing the Zr-aspartate crystal structure, Fig. 6, modified with pendant thiol groups protruding into the cages of the MOF clearly support this conclusion.

Comparing the uptake capacity of **1** towards Cd(II) and Pb(II), to those previously reported in the literature, indicated a high capacity of **1** as compared to other systems, Fig. 7. In case of Pb(II), **1** outperformed all comparable sorbents, including $Zn(ABD)L_{0.5}\cdot 1.5$ DMF (463.52 mg g^{-1}) and TIF-A1/chitosan (397.3 mg g^{-1}), confirming the significance of the strong affinity of the thiol groups from the linkers for soft metal ions.[31,32] For Cd(II) removal, **1** demonstrated superior performance compared to most materials such as FJI-H9 (286 mg g^{-1}) and MOF-808@PAN (225 mg g^{-1}), surpassed only by MOF-808- EDTA (528 mg g^{-1}) which incorporated multi-dentate EDTA chelating ligands.[33–35]

Despite the existence of adsorbents with comparable or even high adsorption capacities, such as EDTA-functionalized MOFs, the synthesis of **1** was notably more efficient, sustainable, and cost-effective. It was synthesized using the inexpensive, readily available mercaptosuccinic acid (MSA) in water as a green solvent, eliminating the need for toxic organic reagents and reducing the synthesis time to just 2 hours. In contrast, many other MOFs relied on complex, costly ligands and required longer reaction times, up to 24 hours in hazardous solvents.

Fast adsorption kinetics of Zr-MSA-MA MOF

To investigate how rapidly equilibrium is established when crystals of **1** are introduced into a solution of heavy metal ions, a time-dependent study was conducted. The concentration of heavy metal ions in solution was monitored by analyzing aliquots of the solution in 30 minute intervals. Results indicated fast uptake by the MOF within the first 30 minutes, reaching almost 80% of the total uptake, eventually reaching equilibrium within 90 minutes. This was due to the incorporation of the alkyl thiol groups that provided a strong affinity for heavy metals, enabling fast uptake kinetics, Fig. 8.

Three kinetic models were employed to evaluate the adsorption behavior of Cd(II) and Pb(II) ions in **1**. The pseudo-first-order (PFO) and pseudo-second-order (PSO) models were applied to determine whether the adsorption process is primarily influenced by the metal ion concentration, the amount of adsorbent, or both.[36] To further investigate the contribution of diffusion mechanisms during adsorption, the DB-model was also utilized[37,38] The mathematical expressions of these models, along with their corresponding parameters, are presented in Table 1.

The fitted kinetic parameters and adsorption capacities are presented in Table 2. For all three metals, both models showed worthy agreement with the experimental data, Fig. 9. However, the PFO model exhibited slightly better accuracy in estimating the equilibrium adsorption capacity (q_e), with lower Δq_e% values across all cases (Cd: 0.5%, Pb: 0.5%) compared to the PSO model (Cd: 6.7%, Pb: 2.5%). This suggests that the PFO model better describes the adsorption kinetics under the applied conditions. Nevertheless, the PSO model also provided a reasonable fit, particularly for Pb. Overall, these findings

Table 1 The mathematical expressions for the three models utilized to fit the adsorption data for Cd(II) and Pb(II) in **1**

Model	Equation	Parameters
PFO	$q_t = q_e(1 - e^{-k_1 t})$	q_t: adsorbed amount at time t (mg g^{-1}), q_e: adsorbed amount at equilibrium (mg g^{-1}), k_1: PFO-rate constant (h^{-1}), k_2: PSO-rate constant (g mg^{-1} h^{-1})
PSO	$q_t = \frac{k_2 q_e^2 t}{1 + k_2 q_e t}$	
DB	$(C_f\, C_e/C_i) \ln C_t - C_t = St^n - D$	C_f: final concentration (mg l^{-1}), C_e: equilibrium concentration (mg l^{-1}), C_i: initial concentration (mg l^{-1}), S: slope, representing rate constant (k_{DB}), n: diffusion factor, D: integration constant

Table 2 Fitting parameters for PFO and PSO models

Model	Rate constant	Estimated q_e (mg g^{-1})	Experimental q_e (mg g^{-1})
Cd(II)			
PFO	$k_1 = 2.32$ h^{-1}	159.4 ($\Delta q_e\% = 0.5\%$)	160.2
PSO	$k_2 = 0.025$ g mg^{-1} h^{-1}	170.9 ($\Delta q_e\% = 6.7\%$)	
Pb(II)			
PFO	$k_1 = 4.06$ h^{-1}	274.6 ($\Delta q_e\% = 0.5\%$)	276
PSO	$k_2 = 0.044$ g mg^{-1} h^{-1}	282.8 ($\Delta q_e\% = 2.5\%$)	

indicate that the adsorption rates are well represented by both models, with the adsorption rate likely influenced by the amount of adsorbent and the initial metal ion concentration applied under the experimental conditions. The adsorption kinetics of Cd(II) and Pb(II) ions in **1** can be best fitted to a pseudo first order (PFO) model. Data fitting employing the PFO model showed Pb(II) capacity q_e of 274.6 mg g^{-1} (1.32 mmol g^{-1}), and Cd(II) adsorption capacity of 159.4 mg g^{-1} (1.42 mmol g^{-1}). In terms of adsorption rate constants, Pb(II) showed the highest PFO rate constant ($k_1 = 4.06$ h^{-1}), indicating faster initial adsorption kinetics relative to Cd(II) ($k_1 = 2.32$ h^{-1}). As adsorption rate calculations were performed based on mass uptake, and considering the vast difference in molar mass between Cd(II) (112.414 g mol^{-1}) and Pb(II) (207.2 g mol^{-1}), it is evident that Cd(II) diffusion and uptake is more facilitated into **1**. This observation can potentially be attributed to the subtle differences in hydrated metal ion radii, hydration energy, or coordination strength with thiol functional groups on **1**.

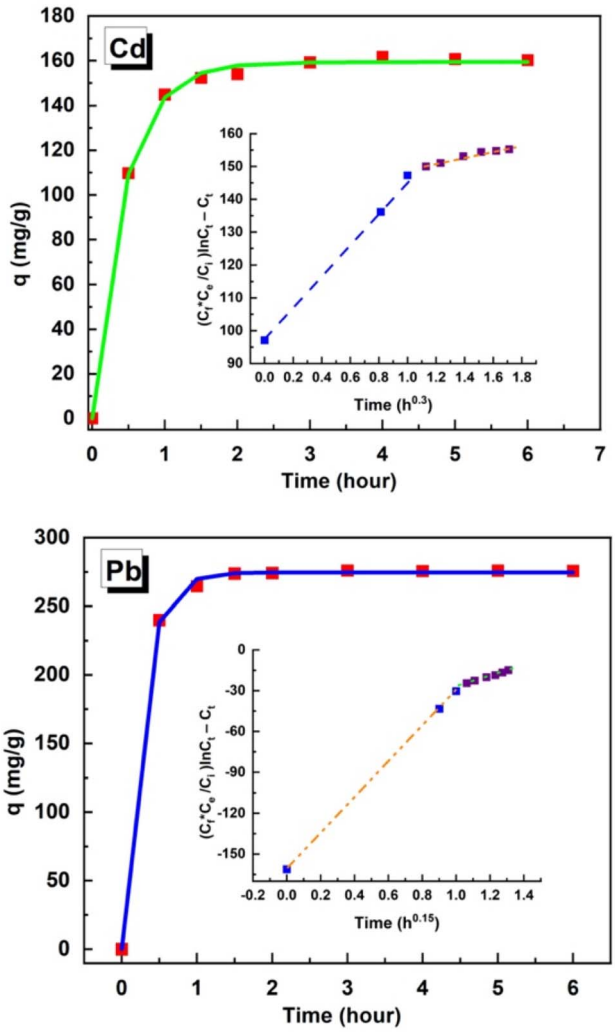

Fig. 9 Pseudo-first order model fitting to the adsorption kinetics of Cd(II) and Pb(II) (line) and DB-kinetics model fitting (inset in the corresponding figure).

To assess the contribution of diffusion mechanisms in the adsorption process, the DB model was applied, and the fitting parameters are presented in Table 3. The S_1/S_2 ratio indicated that surface diffusion plays a dominant role in the overall adsorption process, particularly for Cd ($S_1/S_2 = 6.8$), whereas Pb ($S_1/S_2 = 3.5$) shows a more balanced influence of both surface and intraparticle diffusion. The model also provided accurate prediction for Pb(II) adsorption capacity, with a variance between observed and calculated capacity ($\Delta q\%$) of 6.8%, suggesting that diffusion processes are well-represented for this ion. However, for Cd(II), the model significantly underestimated and miss-estimated the adsorption capacity, with a $\Delta q\%$ value of 25.5%. This discrepancy suggests that the DB model may not fully capture the adsorption dynamics of Cd(II) under the applied experimental conditions. Nonetheless, the results support the general conclusion that surface diffusion is a major controlling factor in the adsorption kinetics for all tested metal ions. It is noteworthy that the values of the diffusion exponent n were consistently low for both metal ions: 0.3 for Cd(II) and 0.15 for Pb(II). The low n values can be attributed to resistance to mass transfer within the sorbent, or limitations in intraparticle diffusion, especially under the experimental conditions applied. Such low n values also align with the dominance of surface diffusion (as indicated by high S_1/S_2 ratios), implying that the adsorption rate is not strongly governed by time-dependent intraparticle diffusion at a later stage.

Furthermore, for both ions, the rate constant associated with the first diffusion region, k_{DB1}, was higher than that of the second region, k_{DB2}. This trend indicates that the initial phase of adsorption proceeds more rapidly, highly likely due to the availability of a large number of active surface sites. As adsorption progresses, the rate decreases (lower k_{DB2}), possibly due to the saturation of surface sites and the increasing role of intraparticle diffusion or pore filling. This two-stage behavior supports the diffusion-controlled mechanism and reinforces the dominance of surface diffusion during the early adsorption phase.

Table 3 Fitting parameters for the DB-model for Cd(II) and Pb(II) in **1**

Species	S_1	S_2	S_1/S_2	n	k_{DB1}	k_{DB2}	q_1	q_2	q_{total}	q_{exp}	$\Delta q\%$
Cd(II)	60.51	8.91	6.8	0.3	14.43	2.80	108.58	10.84	119.43	160.25	25.5
Pb(II)	129.93	37.59	3.5	0.15	19.49	5.64	276.23	18.42	294.65	276.03	6.8

Investigating the pH effect on the Zr-MSA-MA MOF uptake behavior

The effect of solution pH on the capacity of **1** for heavy metal uptake was investigated, Fig. 10, demonstrating optimal uptake at pH = 6 for both Cd(II) and Pb(II) ions. While it is to be expected that thiols, in general, are more acidic than corresponding alcohols, increasing the pH of the medium did not cause a concomitant increase in capacity beyond pH = 6. Indeed, crystals of **1** at lower pH values (2–5) demonstrated diminished capacity towards metal uptake, where capacity decreases with increasing solution acidity. An optimal adsorption capacity was recorded at pH = 6, for Cd(II) and Pb(II), decreasing also when the pH was increased to 8. This behavior can be explained in terms of facilitated deprotonation of the thiol at pH ~6, increasing the available binding sites for heavy metal ions, where above pH 7 hydroxyl ions in the aqueous solution might compete for the heavy metal ions precluding effective uptake into **1**. To test this postulate, zeta potential measurements were made for a suspension of **1** in an aqueous solution of different pH values, Fig. 11. Interestingly, it was noted that crystals of **1** demonstrated increasingly negative surface charge upon increasing the media pH from 4 to 10. As the Zr-carboxylate clusters in **1** are highly oxophilic, it is reasonable to assume hydroxyl ion coordination to the Zr(IV) clusters at such pH values, contributing to the buildup of negative charges on the crystallites of **1**. It is therefore concluded that an optimal solution pH = 6 resulted in adequate buildup of negatively charged cages of **1**, while avoiding competitive masking of Cd(II) and Pb(II) through hydroxyl ion coordination in solution, thus providing the most suitable environment to exploit the full potential of **1** towards Cd(II) and Pb(II) uptake.

Investigating the recyclability of Zr-MSA-MA MOF. The Zr-MSA-MA MOF was found to be highly robust and reusable towards the removal of heavy metal ions from their aqueous solution. After adsorption of the metal ion in a flow-through setup, the MOF can easily be regenerated through acid wash, replenishing the active MOF almost instantaneously. We furthermore attempted 10 consecutive adsorption-regeneration-reuse cycles, for the three metal contaminants investigated herein. The results are shown in Fig. 12, clearly indicating high degree of reusability, and maintained activity for at least 10 consecutive cycles. The Pb(II) exposed MSA-MOF demonstrated the highest recyclability, retaining 95% of the

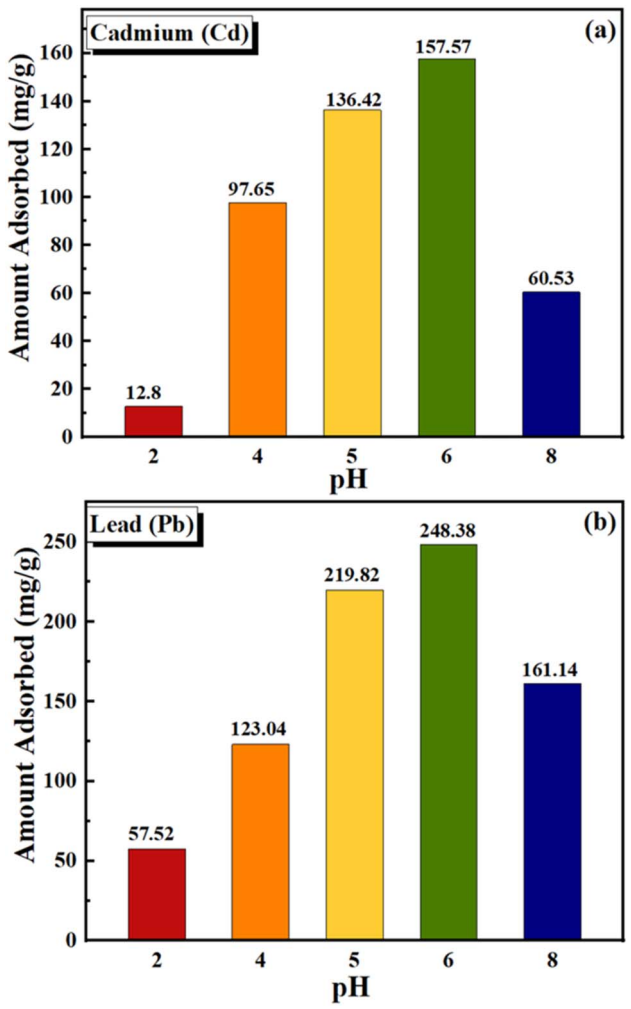

Fig. 10 Effect of pH on the Zr-MSA-MA-MOF capacity towards (a) Cd(II) ions and (b) Pb(II) ions, initial concentration of heavy metals kept at 100 ppm.

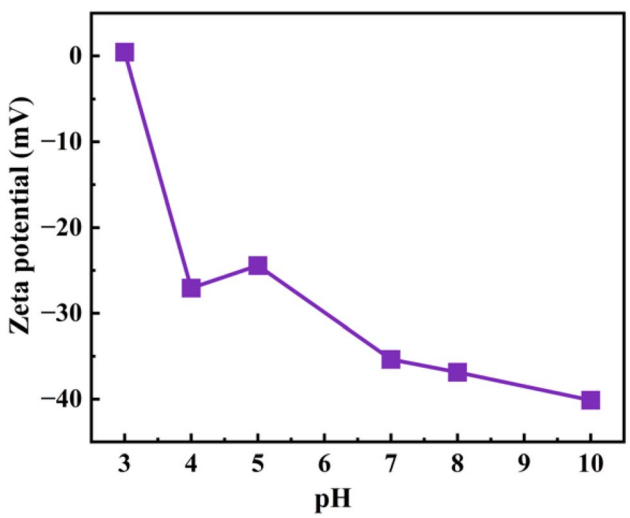

Fig. 11 Measurement of zeta potential for **1** at different pH values, indicating buildup of negative surface charge at pH > 3.

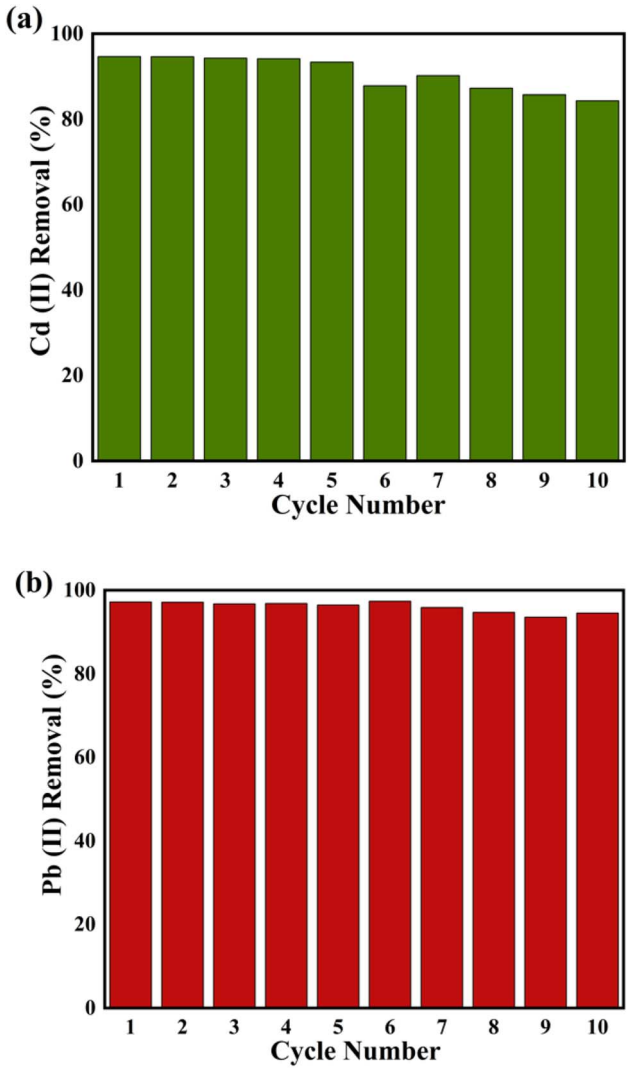

Fig. 12 Ability to regenerate and reuse the Zr-MSA-MA-MOF after adsorption of (a) Cd(II) ions and (b) Pb(II) ions.

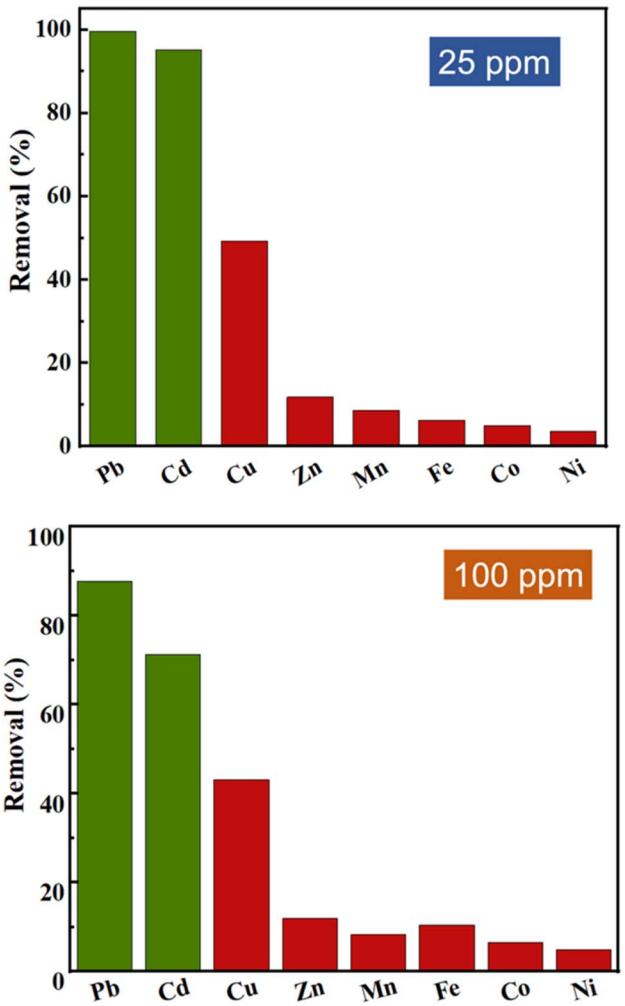

Fig. 13 Ability of Zr-MSA-MA-MOF to selectively capture Cd(II), Pb(II) ions in the presence of competing ions at two different concentration of 10 ppm and 100 ppm for each metal ion.

initial activity after the 10th cycle. This is followed by **1** contacted with Cd(II), retaining 84% of initial activity by the 10th cycle. One plausible explanation of the observed results is the competitive nature of Cd(II) ions towards carboxylate functionality, inducing irreversible damage and structural changes in **1** upon extended exposure to the Cd(II) ions. Despite this seemingly negative impact, we still note that the Zr-MSA-MA MOF still demonstrated exceptionally high potential for heavy metal removal from wastewater with apparent recyclability that justifies its relatively higher cost as compared to moderately active zeolites or ion-exchange resins for this application.

Selective uptake in the presence of competing ions

To probe the selectivity of the thiol-functionalized MOF (**1**) towards soft heavy metal ions, crystals of **1** were introduced into a solution containing Pb, Cd, Zn, Cu, Mn, Fe, and Co ions, from their corresponding nitrate salts, to avoid any interference through precipitation by counterions. After reaching equilibrium, the concentration of all ions in the solution was determined to calculate the removal % for each specific ion, data shown in Fig. 13. At 10 ppm concentration of each different metal ion, **1** demonstrated selective uptake for Pb(II) (99.6% removal), and Cd(II) (95.2% removal), compared to the other metal ions in the same solution (ranging from ~50% removal to as low as 3.5% removal). In a much demanding condition, 100 ppm of each metal ion, compound **1** also demonstrated remarkable selectivity towards Pb(II) (86% removal) and Cd(II) (71% removal), as compared to the rest of competing ions. The data clearly demonstrated the selective removal of soft heavy metal ions in the presence of equal concentration of other metal ions, consistent with expected soft-acid-soft-base interactions between the soft metal ions and the thiol groups lining the cages of **1**. Interestingly, the highest removal % of Cu as compared to the rest of the ions investigated (Zn, Fe, Mn, Co) is in line with this assumption, due to the favorable Cu–S bond formation as compared to the other metal ions. In this study, nitrate counterions were used to avoid precipitation of insoluble metal halides or sulfates, *e.g.* $PbCl_2$, $PbSO_4$, or $CdSO_4$ which will artificially result in apparent removal of Cd(II) or

Pb(II) ions from solution. In a real water stream, presence of chloride and sulfate ions is expected, however this is not expected to affect the preferential uptake of **1** for Pb(II) or Cd(II), presence of such interfering ions will decrease the concentration of water-soluble species rather than interfering with the uptake capability and selectivity of **1**.

Conclusion

In conclusion, we demonstrated that inducing defect sites within the Zr-mercaptosuccinate MOF, along with including the mercaptoacetic acid as a capping ligand in the Zr-cluster is key toward achieving high capacity, high selectivity, and high recyclability of the MOF towards removal of Pb(II) and Cd(II) ions from water. The green, water-based synthesis of the MSA-MOF is considerably appealing for a greener holistic water treatment solution. The pH dependence of metal removal capacity indicated that slightly acidic media is preferred (pH = 6) for highest attainable capacity of the MOF, reflecting a balance between thiol-coordination and hydroxyl binding of metal ions. The MSA-MOF demonstrated extended lifecycle, where ~95% of initial heavy metal uptake capacity was maintained even after 10 consecutive uptake-regeneration cycles. Finally, the MSA-MOF demonstrated notable selectivity towards Pb(II) and Cd(II) removal even in the presence of competing ions including Cu(II), Zn(II), Fe(III), Mn(II), Co(II), and Ni(II), demonstrating significant dependence on soft-acid-soft-base thiolate–metal interactions governing the material performance.

Experimental

Materials

All reagents were of analytical grade and used as received without further purification. The chemicals including $ZrCl_4$, mercaptoacetic acid (MA), and $Cu(NO_3)_2 \cdot 2.5(H_2O)$ were purchased from Sigma-Aldrich. Mercaptosuccinic acid (MSA), formic acid (FA), and ethanol were purchased from Merk. $Cd(NO_3)_2 \cdot 4(H_2O)$ from Acros Organics, $Pb(NO_3)_2$, $Fe(NO_3)_3 \cdot 9(H_2O)$, $Zn(NO_3)_2 \cdot 6(H_2O)$ $Co(NO_3)_2 \cdot 6H_2O$, $Ni(NO_3)_2 \cdot 6(H_2O)$ from Fisher Scientific, UK. Deionized water (DI) was used to prepare the solutions (MilliQ).

Characterization

Fourier transform Infrared (FTIR) spectroscopy was conducted on ThermoScientific iQ-10. Scanning, electron microscopy (SEM) was conducted on Thermofisher (USA) Quattro S Field Emission Gun, Environmental SEM (FEGSEM). X-ray diffraction (XRD) patterns were acquired on a Bruker powder diffractometer equipped with Cu Kα radiation (35 kV, 15 mA) at a scan rate of 10° min^{-1} with step width 0.015° and Scan range 5–80°. Inductively coupled plasma mass spectrometer (ICP-MS) was employed to determine the content of various elements in aqueous solutions.

Synthesis of Zr-MSA

In a clean, dry scintillation vial, $ZrCl_4$ (150 mg, 0.64 mmol), MSA (100 mg, 0.66 mmol), and 100 μL of formic acid (FA, 4 eq. relative to $ZrCl_4$) were combined in 2 mL of DI water and sonicated for 10 minutes. Then, the mixture was kept in thermal block at 80 °C. After 2 hours, the reaction mixture was cooled down to room temperature, and the white precipitate was collected by centrifugation, followed by washing with 10 mL of DI water (twice) then 10 mL of ethanol (three times). Finally, the solid was dried under a vacuum at 60 °C overnight. (Yield = 160 mg).

Synthesis of Zr-MSA-MA

In a clean, dry scintillation vial, $ZrCl_4$ (125 mg, 0.53 mmol), MSA (80 mg, 0.53 mmol), 50 μL of MA, and 50 μL of FA were combined in 2 mL of DI water and sonicated for 10 minutes. Then, the mixture was kept in thermal block at 80 °C. After 2 hours, the reaction mixture was cooled down to room temperature, and the white precipitate was collected by centrifugation, followed by washing with 10 mL of DI water (twice) then 10 mL of ethanol (three times). Finally, the solid was dried under a vacuum at 60 °C overnight. (Yield = 130 mg).

Kinetics studies

Cadmium. In eight sealed glass vials,10.5 mg of Zr-MSA-MA was left to stir at room temperature with 20 mL of 200 ppm Cd(II) for specific time intervals (0.5, 1, 1.5, 2, 3, 4, 5, and 6 hours). After each time interval, the supernatant was collected from each vial separately by centrifugation at 6000 rpm for 10 minutes, followed by microfiltration membrane (pore size, 0.22 μm). The Cd(II) concentration in the supernatant was then measured using an inductively coupled plasma mass spectrometer (ICP-MS).

Lead. In eight sealed glass vials,10.5 mg of Zr-MSA-MA was left to stir at room temperature with 20 mL of 200 ppm Pb(II) for different time intervals (0.5, 1, 1.5, 2, 3, 4, 5, and 6 hours). After each time interval, the supernatant was collected from each vial separately by centrifugation at 6000 rpm for 10 minutes, followed by microfiltration membrane (pore size, 0.22 μm). The Pb(II) concentration in the supernatant was then measured using an inductively coupled plasma mass spectrometer (ICP-MS).

Dose-dependency studies

Cadmium. In five sealed glass vials, different weights of Zr-MSA-MA (5, 10, 20, 30 and 40 mg) was left to stir at room temperature with 20 mL of 200 ppm Cd(II) for 4 h. After which, the supernatant was collected from each vial separately by centrifugation at 6000 rpm for 10 minutes, followed by microfiltration membrane (pore size, 0.22 μm). The Cd(II) concentration in the supernatant was then measured using an inductively coupled plasma mass spectrometer (ICP-MS).

Lead. In five sealed glass vials, different weights of Zr-MSA-MA (5, 10, 20, 30 and 40 mg) was left to stir at room temperature with 20 mL of 200 ppm Pb(II) for 4 h. After which, the supernatant was collected from each vial separately by centrifugation at 6000 rpm for 10 minutes, followed by microfiltration

membrane (pore size, 0.22 μm). The Pb(II) concentration in the supernatant was then measured using an inductively coupled plasma mass spectrometer (ICP-MS).

pH-dependency studies

Cadmium. In five sealed glass vials, 10.5 mg of Zr-MSA-MA was left to stir at 450 rpm at room temperature with 20 mL of 200 ppm Cd(II) of different pH (2, 4, 5, 6, and 8). After 4 h, the supernatant was collected from each vial separately by centrifugation at 6000 rpm for 10 minutes, followed by microfiltration membrane (pore size, 0.22 μm). The Cd(II) concentration in the supernatant was then measured using an inductively coupled plasma mass spectrometer (ICP-MS).

Lead. In five sealed glass vials, 10.5 mg of Zr-MSA-MA was left to stir at 450 rpm at room temperature with 20 mL of 200 ppm Pb(II) of different pH (2, 4, 5, 6, and 8). After 4 h, the supernatant was collected from each vial separately by centrifugation at 6000 rpm for 10 minutes, followed by microfiltration membrane (pore size, 0.22 μm). The Pb(II) concentration in the supernatant was then measured using an inductively coupled plasma mass spectrometer (ICP-MS).

The desired pH of each stock solution was adjusted through the addition of either 0.1 M HCl or NaOH.

Adsorption isotherm studies

Cadmium. In sealed glass vials, eight separate samples of 10.5 mg Zr-MSA-MA was added into 20 mL of Cd(II) solutions of different concentrations (25, 50, 100, 200, 400, 600, 800, 1000 ppm) and stirred at 450 rpm (pH = 6). After 4 h, the supernatant from each vial was separately collected by centrifugation at 6000 rpm for 10 minutes, followed by microfiltration membrane (pore size, 0.22 μm). The Cd(II) concentration in the supernatant was then measured using an inductively coupled plasma mass spectrometer (ICP-MS).

Lead. In sealed glass vials, eight separate samples of 10.5 mg Zr-MSA-MA was added into 20 mL of Pb(II) solutions of different concentrations (25, 50, 100, 200, 400, 600, 800, 1000 ppm) and stirred at 450 rpm (pH = 6). After 4 h, the supernatant was collected from each vial separately by centrifugation at 6000 rpm for 10 minutes, followed by microfiltration membrane (pore size, 0.22 μm). The Pb(II) concentration in the supernatant was then measured using an inductively coupled plasma mass spectrometer (ICP-MS).

Regeneration studies

Cadmium. To probe the regeneration ability of Zr-MSA-MA MOF, a 0.45 μm nylon syringe filter was loaded with 30 mg of Zr-MSA-MA after being suspended in 10 mL of DI water. Then, 20 mL of 15 ppm of Cd(II) solution was passed through the loaded syringe filter, and the filtrate was collected for ICP analysis. The syringe filter was then washed with 1 M HCl (20 mL) followed by 20 mL of DI water. The Cd^{2+} uptake and washing were repeated for 10 cycles.

Lead. To probe the regeneration ability of Zr-MSA-MA MOF, a 0.45 μm nylon syringe filter was loaded with 30 mg of Zr-MSA-MA after being suspended in 10 mL of DI water. Then, 20 mL of 15 ppm of Pb(II) solution was passed through the loaded syringe filter, and the filtrate was collected for ICP analysis. The syringe filter was then washed with 1 M HCl (20 mL) followed by 20 mL of DI water. The Pb(II) uptake and washing were repeated for 10 cycles.

Selectivity studies

The effect of competing ions on the uptake efficiency was investigated using a batch-ion exchange protocol in which 40 mg of Zr-MSA-MA was immersed in mixture made by mixing 5 mL of 25 ppm from each of the following metal ions: Pb(II), Cd(II), Cu(II), Zn(II), Mn(II), Fe(III), Co(II), and Ni(II) with stirring. After 4 h, the supernatants were collected by centrifugation followed by microfiltration for determining the concentration of each ion using an inductively coupled plasma mass spectrometer (ICP-MS). The same procedure was repeated but utilizing 100 ppm of each metal ion to test the selectivity in more demanding environment.

Conflicts of interest

There are no conflicts to declare.

Data availability

The datasets supporting this article have been uploaded as part of the manuscript and the supplementary information (SI). Supplementary information is available. See DOI: https://doi.org/10.1039/d5su00859j.

Acknowledgements

This paper is based upon work supported by Science, Technology & Innovation Funding Authority (STDF) under grant 48419. The authors also acknowledge the financial support from the Academy of Scientific Research and Technology (ASRT-P2P).

References

1 F. Florides, M. Giannakoudi, G. Ioannou, D. Lazaridou, E. Lamprinidou, N. Loukoutos, M. Spyridou, E. Tosounidis, M. Xanthopoulou and I. A. Katsoyiannis, Water reuse: A comprehensive review, *Environments*, 2024, **11**(4), 81.
2 A. Abou-Shady, M. S. Siddique and W. Yu, A critical review of recent progress in global water reuse during 2019–2021 and perspectives to overcome future water crisis, *Environments*, 2023, **10**(9), 159.
3 S. Das, C. K. Singh, K. K. Sodhi and V. K. Singh, Circular economy approaches for water reuse and emerging contaminant mitigation: innovations in water treatment, *Environ. Dev. Sustain.*, 2023, 1–42.
4 P. Saravanan, V. Saravanan, R. Rajeshkannan, G. Arnica, M. Rajasimman, B. Gurunathan and A. Pugazhendhi, Comprehensive review on toxic heavy metals in the aquatic system: sources, identification, treatment strategies, and health risk assessment, *Environ. Res.*, 2024, 119440.

5 M. Balali-Mood, K. Naseri, Z. Tahergorabi, M. R. Khazdair and M. Sadeghi, Toxic mechanisms of five heavy metals: mercury, lead, chromium, cadmium, and arsenic, *Front. Pharmacol.*, 2021, **12**, 643972.
6 M. Yadav, R. Gupta and R. K. Sharma, Green and sustainable pathways for wastewater purification, In *Advances in Water Purification Techniques*, Elsevier, 2019, pp 355–383.
7 Z. Jeirani, C. H. Niu and J. Soltan, Adsorption of emerging pollutants on activated carbon, *Rev. Chem. Eng.*, 2017, **33**(5), 491–522.
8 L. Swatuk, M. McMorris, C. Leung and Y. Zu, Seeing "invisible water": challenging conceptions of water for agriculture, food and human security, *Can. J. Dev. Stud.*, 2015, **36**(1), 24–37.
9 T. O. Ajiboye, O. A. Oyewo and D. C. Onwudiwe, Simultaneous removal of organics and heavy metals from industrial wastewater: A review, *Chemosphere*, 2021, **262**, 128379.
10 A. H. Ibrahim, R. R. Haikal, R. S. Eldin, W. A. El-Mehalmey and M. H. Alkordi, The Role of Free-Radical Pathway in Catalytic Dye Degradation by Hydrogen Peroxide on the Zr-Based UiO-66-NH2 MOF, *ChemistrySelect*, 2021, **6**(42), 11675–11681.
11 A. Hani, R. R. Haikal, W. A. El-Mehalmey, Y. Safwat and M. H. Alkordi, Durable and recyclable MOF@ polycaprolactone mixed-matrix membranes with hierarchical porosity for wastewater treatment, *Nanoscale*, 2023, **15**(48), 19617–19628.
12 T. Hashem, E. P. V. Sanchez, E. Bogdanova, A. Ugodchikova, A. Mohamed, M. Schwotzer, M. H. Alkordi and C. Wöll, Stability of monolithic mof thin films in acidic and alkaline aqueous media, *Membranes*, 2021, **11**(3), 207.
13 T. Hashem, E. P. Valadez Sánchez, P. G. Weidler, H. Gliemann, M. H. Alkordi and C. Wöll, Liquid-phase quasi-epitaxial growth of highly stable, monolithic UiO-66-NH2 MOF thin films on solid substrates, *ChemistryOpen*, 2020, **9**(5), 524–527.
14 S. Wang, M. Wahiduzzaman, L. Davis, A. Tissot, W. Shepard, J. Marrot, C. Martineau-Corcos, D. Hamdane, G. Maurin and S. Devautour-Vinot, A robust zirconium amino acid metal-organic framework for proton conduction, *Nat. Commun.*, 2018, **9**(1), 4937.
15 Z. Baocheng, L. Guo, W. Shixing, H. Tu, A. Yunfei and z. Libo, Metal-organic frameworks for sustainable recovery of precious metals: Advances in synthesis, applications and multiscale mechanisms, *Int. J. Miner. Process.*, 2025, **33**(2), 417–445.
16 Z. Gao, K. Yang, Z. Zhao, D. Lan, Q. Zhou, J. Zhang and H. Wu, Design principles in MOF-derived electromagnetic wave absorption materials: Review and perspective, *Int. J. Min. Met. Mater.*, 2023, **30**(3), 405–427.
17 S. Begum, R. R. Haikal, A. H. Ibrahim, M. A. Safy, M. Tsotsalas and M. H. Alkordi, Flash synthesis for conformal monolithic coatings of the Zr-based metal-organic framework (UiO-66-NH2) on non-modified surfaces: Applications in thin-film electrode systems, *Surf. Interfaces*, 2020, **20**, 100587.
18 M. H. Hassan, R. R. Haikal and M. H. Alkordi, Synergistic compounding of carbon nanotubes and metal–organic frameworks for oxygen-evolving electrocatalysis, *Mater. Adv.*, 2022, **3**(19), 7212–7218.
19 M. E. Safy, M. Amin, R. R. Haikal, B. Elshazly, J. Wang, Y. Wang, C. Wöll and M. H. Alkordi, Probing the water stability limits and degradation pathways of metal–organic frameworks, *Chem.–Eur. J.*, 2020, **26**(31), 7109–7117.
20 Z. Han, Y. Yang, J. Rushlow, J. Huo, Z. Liu, Y.-C. Hsu, R. Yin, M. Wang, R. Liang, K.-Y. Wang and H.-C. Zhou, Development of the design and synthesis of metal–organic frameworks (MOFs) – from large scale attempts, functional oriented modifications, to artificial intelligence (AI) predictions, *Chem. Soc. Rev.*, 2025, **54**(1), 367–395.
21 D. Prat, A. Wells, J. Hayler, H. Sneddon, C. R. McElroy, S. Abou-Shehada and P. J. Dunn, CHEM21 selection guide of classical- and less classical-solvents, *Green Chem.*, 2016, **18**(1), 288–296.
22 H. Luo, F. Cheng, L. Huelsenbeck and N. Smith, Comparison between conventional solvothermal and aqueous solution-based production of UiO-66-NH2: Life cycle assessment, techno-economic assessment, and implications for CO2 capture and storage, *J. Environ. Chem. Eng.*, 2021, **9**(2), 105159.
23 S. Daliran, A. R. Oveisi, C.-W. Kung, U. Sen, A. Dhakshinamoorthy, C.-H. Chuang, M. Khajeh, M. Erkartal and J. T. Hupp, Defect-enabling zirconium-based metal–organic frameworks for energy and environmental remediation applications, *Chem. Soc. Rev.*, 2024, **53**, 6244–6294.
24 P. Yang, Y. Shu, Q. Zhuang, Y. Li and J. Gu, A robust MOF-based trap with high-density active alkyl thiol for the super-efficient capture of mercury, *Chem. Commun.*, 2019, **55**(86), 12972–12975.
25 L. Beyer, R. Kirmse, J. Stach, R. Szargan and E. Hoyer, Metallkomplexe des Benzoyldithioessigsäuremethylesters und des N-Benzoylamino-dithiokohlensäureethylesters: Darstellung und Charakterisierung, ESCA- und EPR-Untersuchungen [1], *Z. Anorg. Allg. Chem.*, 1981, **476**(5), 7–15.
26 E. Agostinelli, C. Battistoni, D. Fiorani, G. Mattogno and M. Nogues, An XPS study of the electronic structure of the ZnxCd1−xCr2(X = S, Se) spinel system, *J. Phys. Chem. Solids*, 1989, **50**(3), 269–272.
27 A. R. H. F. Ettema and C. Haas, An X-ray photoemission spectroscopy study of interlayer charge transfer in some misfit layer compounds, *J. Phys.: Condens. Matter*, 1993, **5**(23), 3817.
28 H. Jenkins and K. Thakur, Reappraisal of thermochemical radii for complex ions, *J. Chem. Educ.*, 1979, **56**(9), 576.
29 J. W. Arblaster, *Selected Values of the Crystallographic Properties of Elements*, ASM International, 2018.
30 S. Wang, M. Wahiduzzaman, L. Davis, A. Tissot, W. Shepard, J. Marrot, C. Martineau-Corcos, D. Hamdane, G. Maurin, S. Devautour-Vinot and C. Serre, A robust zirconium amino acid metal-organic framework for proton conduction, *Nat. Commun.*, 2018, **9**(1), 4937.

31 C.-X. Yu, K.-Z. Wang, X.-J. Li, D. Liu, L.-F. Ma and L.-L. Liu, Highly efficient and facile removal of Pb2+ from water by using a negatively charged azoxy-functionalized metal–organic framework, *Cryst. Growth Des.*, 2020, **20**(8), 5251–5260.

32 Y. Ma, D. You, Y. Fang, J. Luo, Q. Pan, Y. Liu, F. Wang and W. Yang, Confined growth of MOF in chitosan matrix for removal of trace Pb (II) from reclaimed water, *Sep. Purif. Technol.*, 2022, **294**, 121223.

33 H. Xue, Q. Chen, F. Jiang, D. Yuan, G. Lv, L. Liang, L. Liu and M. Hong, A regenerative metal–organic framework for reversible uptake of Cd (II): from effective adsorption to in situ detection, *Chem. Sci.*, 2016, **7**(9), 5983–5988.

34 J. E. Efome, D. Rana, T. Matsuura and C. Q. Lan, Insight studies on metal-organic framework nanofibrous membrane adsorption and activation for heavy metal ions removal from aqueous solution, *ACS Appl. Mater. Interfaces*, 2018, **10**(22), 18619–18629.

35 Y. Peng, H. Huang, Y. Zhang, C. Kang, S. Chen, L. Song, D. Liu and C. Zhong, A versatile MOF-based trap for heavy metal ion capture and dispersion, *Nat. Commun.*, 2018, **9**(1), 187.

36 Y. S. Ho and G. McKay, Pseudo-second order model for sorption processes, *Process Biochem.*, 1999, **34**(5), 451–465.

37 A. Baraka, A novel kinetic model for batch aqueous-solution/porous-solid adsorption systems, *Desalination Water Treat.*, 2014, **52**(28), 5343–5356.

38 A. Baraka, Investigation of temperature effect on surface-interaction and diffusion of aqueous-solution/porous-solid adsorption systems using diffusion–binding model, *J. Environ. Chem. Eng.*, 2015, **3**(1), 129–139.